mathematics

MDPI

Article

Modeling and Structural Analysis of MEMS Shallow Arch Assuming Multimodal Initial Curvature Profiles

Ayman M. Alneamy [1] and Hassen M. Ouakad [2,*]

[1] Department of Mechanical Engineering, Jazan University, Jazan 45142, Saudi Arabia; alneamy@jazanu.edu.sa
[2] Renewable Energy Engineering Department, Mediterranean Institute of Technology, South Mediterranean University, les Berges du Lac 2, Tunis 1053, Tunisia
* Correspondence: hassen.ouakad@medtech.tn

Abstract: The present investigation focuses on the design and mathematical modeling of a microelectromechanical (MEMS) mode-localized based sensor/actuator system. This device incorporates a sensitive clamped–clamped shallow arch microbeam with an initial curvature shaped to resemble one of the first two symmetric and asymmetric modes of free oscillations of a clamped–clamped beam. The analysis reveals that with a suitable arrangement of the initial shape of the device flexible electrode and a proper tuning of the maximum initial rise and the actuating dc load enables the transition to display certain bistable behavior. This could be a better choice to build a device with a large stroke. Furthermore, the generated data showed the occurrence of mode-veering, indicating a coupling between the concerned symmetric and asymmetric modes of vibrations, and offering the possibility for such a device to be used as a mode-localized MEMS-based sensor utilizing veering and crossing phenomena. Indeed, where a certain energy is exchanged between symmetric and asymmetric modes of a microbeam, it can be utilized to serve as a foundation for the development of a new class of highly precise resonant sensors that can capture, with a certain level of precision, any of the sensed signal amplitudes.

Keywords: microbeam; shallow arch; snap-through; mode-veering; mode-crossing

MSC: 74H45

check for updates

Citation: Alneamy, A.M.; Ouakad, H.M. Modeling and Structural Analysis of MEMS Shallow Arch Assuming Multimodal Initial Curvature Profiles. *Mathematics* **2024**, *12*, 970. https://doi.org/10.3390/math12070970

Academic Editor: Carlos Conceicao Antonio

Received: 4 March 2024
Revised: 20 March 2024
Accepted: 22 March 2024
Published: 25 March 2024

Copyright: © 2024 by the authors. Licensee MDPI, Basel, Switzerland. This article is an open access article distributed under the terms and conditions of the Creative Commons Attribution (CC BY) license (https://creativecommons.org/licenses/by/4.0/).

1. Introduction

The utilization of inherently nonlinear characteristics within oscillating engineered micro- and nanostructures is becoming increasingly prevalent in the MEMS and NEMS (micro- and nanoelectromechanical system) community. This innovative approach has shown tremendous potential in significantly enhancing the precision and stability of measurements across a broad range of physical micro- and nanosensors [1]. Applied and theoretical research advancements in exploring modal interactions within nonlinear and loosely coupled oscillatory microsystems featuring two or more degrees of freedom are currently experiencing continuous progress.

As an illustration, there is a recent proposal introducing innovative designs for highly sensitive components intended for use in micromechanical inertial MEMS sensors. These components are being engineered to ensure stability even when functioning in environments characterized by significant vibration and temperature variations. To cite a few examples in the MEMS community, in addition to relying on the conventional amplitude modulation techniques [2], there is a significant drive toward using resonant and mode-localized sensors [3]. In reality, MEMS sensors that are based on the mode-localized principle rely on the detection of changes in the vibrational mode of two interconnected resonators in order to determine and measure the oscillation of the micromechanical structure [4]. These sensors make use of the phenomenon of mode localization and rely on

detecting alterations in the vibrational mode of these resonators in order to identify and measure the oscillation of the micromechanical structure.

The investigation of the distinctive modal and resonant characteristics exhibited by micromechanical systems featuring certain geometric perturbations, such as initial curvature in shallow arched microbeams, holds significant interest in the scientific and industrial MEMS and NEMS areas. These properties are harnessed for precision measurements across various domains of study. Certain studies have showcased the successful practical application of such mechanical architectures for high-precision measurements, encompassing parameters like force/transnational acceleration [5], displacements [6], velocity [7], and gas sensors [8,9].

Furthermore, few groups have explored employing systems with initial curvature as actuators [10] and as logical components in advanced computing devices [11]. Currently, in the majority of these designed microdevices, a microbeam with initial curvature serves as a sensitive element, known for its bistable behavior when subjected to a constant electric field within the interelectrode gap. A bistable phenomenon exists in microbeams that are initially curved, exhibiting an oscillatory behavior between two states due to a snap-through mechanism. These structures also have the potential to produce complex nonlinear phenomena such as dynamic snap-through, mode-veering, and mode-crossing [12].

The modeling and design of such macro- and micromechanical structures require the utilization of complicated geometrically and physically nonlinear models that account for the elastic deformation of continuous systems [13]. A substantial number of references in the current literature are dedicated to addressing such issues and challenges [11,14–20]. Furthermore, a distinct and rapidly advancing research domain involves investigating the nonlinear statics and dynamics of macro- and micromechanical structures featuring geometric perturbations exposed to electric fields of varying configurations. More specifically, numerous studies delve into topics like branching, bifurcations, the disruption of equilibrium positions, and the transition between different operating modes for microbeams exhibiting initial curvature [21–26]. Extensive research efforts also focus on exploring the spectral properties and nonlinear dynamic characteristics of such structures [27–32].

In a recent study, Morozov et al. [33] explored the effects of initial curvature amplitude and shape on static equilibrium positions under electrostatic and thermal influences, utilizing a geometrically nonlinear model of a Bernoulli–Euler beam. Additionally, the same research group [34] employed numerical methods and bifurcation-based theory, considering both symmetric and asymmetric lower modes of free vibrations, to investigate the potential use of these structures as sensitive elements in high-precision mode-localized resonant microaccelerometers.

In one of the authors' previous investigation [26], we investigated the phenomenon of mode localization within a microbeam featuring initial curvature, examining the interaction between symmetric and asymmetric vibration modes. We explored scenarios involving symmetrical initial curvature and various electrostatic loading conditions, including situations with asymmetric fields that induce localization as per the specified forms. The reported results showed that the localization phenomenon is observed when oscillations are triggered by a symmetric field, even though the microbeam has an asymmetric initial curvature.

In this work, we investigate the details of a particular MEMS shallow arch through proposing a comprehensive model that considers multimodal initial and counter curvature profiles. Our research builds upon the existing literature, acknowledging similarities in certain aspects while distinctly contributing novel insights to the field. By referencing relevant studies in our extensive list in the bibliography section below, we establish a strong foundation for our work and strive to provide a comprehensive perspective on the structural behavior of MEMS shallow arches. This examination introduces innovative elements that distinguish it from previous works. We move beyond conventional analyses by incorporating multimodal initial curvature profiles into the structural modeling of MEMS shallow arches, offering a nuanced understanding of their behavior. This novel

approach enhances the accuracy of our predictions and contributes valuable knowledge to the broader MEMS research community.

In addition, the study is involved a comprehensive exploration of the nonlinear characteristics in both the static behavior and the variations of the linearized eigenvalue problem for an initially curved microbeam. It also examines the influence of the initial shape arrangement of the shallow arch microbeam on the overall performance of such a structure. Indeed, we explore the potential of constructing MEMS sensors that employ the mode-localization principle, through the manipulation of the beam's profile and arrangement of its shape. This has the potential to result in mode-veering/crossing, thereby triggering the occurrence of the mode-localization phenomenon.

2. Mathematical Model

We next present an analytical model for the electrostatic initially curved microresonator, shown in Figure 1, using Euler–Bernoulli beam theory. The primary limitations of the Euler–Bernoulli beam theory encompass the presumptions of small deflections, linear elasticity, and uniform cross-sectional properties. The curved microbeam has the following dimensions:

$$l_b = 1000\ \mu\text{m} \quad , \quad b = 30\ \mu\text{m} \quad , \quad h = 3\ \mu\text{m},$$

while the capacitor gap between the side-wall electrode (SWD) and the center line is set to $d = 11.5\ \mu$m. The selected material Young's modulus (E) is set to 129 GPa, and its density (ρ) is set to 2332 kg/m^3.

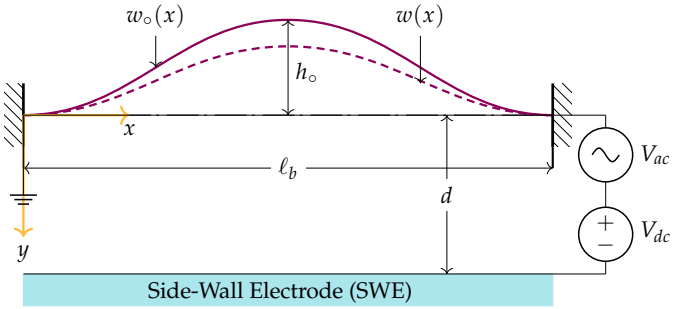


Figure 1. 1D drawing showing the proposed resonator and its electrical connection components. It is excited by a static voltage and a time-varying signal.

Following [35], the equation of motion governs the transverse response of the resonator, which is adopted by adjusting the initial rise and beam profile to resemble one of the first two symmetric and asymmetric modes of free oscillations of a doubly-clamped beam as

$$\rho A\ddot{\bar{w}} + c_v\dot{\bar{w}} + EI_b\bar{w}^{iv} - (w_\circ'' - \bar{w}'')\frac{EA_b}{2\ell_b}\int_0^{\ell_b}(2w_\circ'\bar{w}' - \bar{w}'^2)dx = \frac{\epsilon\, b_b V(t)^2}{2(d + w_\circ - \bar{w})^2} \tag{1}$$

where the boundary conditions of such a structure are the displacement, and slop at both ends are zero. Hence, it is subject to the following boundary conditions:

$$\bar{w}(0) = 0, \qquad \bar{w}'(0) = 0, \qquad \bar{w}(\ell_b) = 0, \qquad \bar{w}'(\ell_b) = 0$$

where c_v is the viscous damping coefficient in the transverse direction. This microresonator features an initial curvature, shown in Figure 1, as

$$w_\circ(\bar{x}) = \pm\frac{h_\circ}{2}\Big(1 - \cos(2\pi\bar{x})\Big) \tag{2}$$

and it is also tailored to mimic the first in-plane symmetric mode shape $\phi_1(x)$, marked as red lines in Figure 2, as

$$w_{o1}(\bar{x}) = \pm\, h_\circ\, \phi_1(\bar{x}) \tag{3}$$

and for the first antisymmetric in-plane mode shape $\phi_2(x)$, illustrated as gold lines in Figure 2 as

$$w_{o2}(\bar{x}) = \pm\, h_\circ\, \phi_2(\bar{x}) \tag{4}$$

as well as for the second symmetric in-plane mode shape $\phi_3(x)$ and defined as black lines in Figure 2

$$w_{o3}(\bar{x}) = \pm\, h_\circ\, \phi_3(\bar{x}) \tag{5}$$

These initial curvature profiles and the initial counter-curvature profiles of the beam are illustrated as solid and dashed lines, respectively, in the following Figure 2.

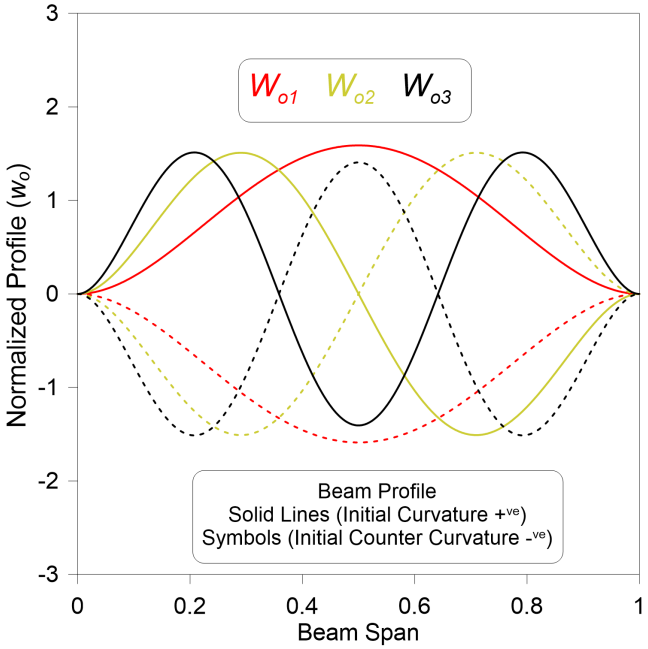


Figure 2. The micro-resonator features an initial curvature mimicking: first in-plane mode shape (ϕ_1), first in-plane antisymmetric mode shape (ϕ_2), and second in-plane symmetric mode shape (ϕ_3). Solid lines represent initial positive curvatures and dashed lines represent initial negative curvatures.

Then, we nondimensionalize the equation of motion governing the resonator transverse response, Equation (1). Toward this, we introduce the following nondimensional parameters:

$$\hat{w} = \frac{\bar{w}}{d}, \qquad \hat{w}_\circ = \frac{w_\circ}{d}, \qquad \hat{x} = \frac{\bar{x}}{l_b}, \qquad t = \frac{\hat{t}}{T}$$

where $T = \sqrt{\rho A {\ell_b}^4 / EI}$ is a time scale. Substituting the nondimensional parameters into Equation (1), and multiplying both sides by $(T^2/d\rho A)$, yields

$$\ddot{\hat{w}} + (\hat{c}_v + \hat{c}_{sq})\dot{\hat{w}} + \hat{w}^{iv} - \alpha_1(\hat{w}_\circ'' - \hat{w}'')\int_0^1 (2\hat{w}_\circ'\hat{w}' - \hat{w}'^2)d\hat{x} = \alpha_2 \frac{V(t)^2}{(1+\hat{w}_\circ - \hat{w})^2} \tag{6}$$

subject to the boundary conditions

$$\hat{w}(0) = 0, \quad \hat{w}'(0) = 0, \quad \hat{w}(1) = 0, \quad \hat{w}'(1) = 0 \tag{7}$$

The nondimensional coefficients appearing in Equation (6) are defined as

$$\alpha_1 = 6\Big(\frac{d}{h_b}\Big)^2, \quad \alpha_2 = \frac{6\epsilon\ell_b^4}{Eh^3d^3}, \quad \hat{c}_{vt} = \frac{c_v\ell_b^4}{EI_bT} \tag{8}$$

therefore, dropping the over-hat for the sake of simplicity, the nondimensional initial curvature $w_\circ(x)$ utilizing four different profiles are expressed as

$$w_\circ(x) = \pm\frac{h_\circ}{2d}\Big(1 - \cos(\frac{2\pi x}{\ell_b})\Big) \tag{9}$$

The first in-plane symmetric mode shape is normalized at the central node as

$$w_\circ(x) = \pm\frac{h_\circ}{d}\Big[\frac{\phi_1(x)}{\phi_1(0.5)}\Big]$$

and $w_\circ(x)$ utilizing the first in-plane antisymmetric profile is normalized at the quarter of the beam span and can be expressed as

$$w_\circ(x) = \pm\frac{h_\circ}{d}\Big[\frac{\phi_2(x)}{\phi_2(0.25)}\Big]$$

and for the second in-plane symmetric mode, the nondimensional profile is

$$w_\circ(x) = \pm\frac{h_\circ}{d}\Big[\frac{\phi_3(x)}{\phi_3(0.5)}\Big]$$

Reduced-Order Model (ROM)

A reduced-order model (ROM) based on a Galerkin approximation is utilized to discretize the equation of motion in terms of a finite number of degrees of freedom. These must satisfy the boundary conditions. In this case, we chose straight beam mode shapes instead of initially curved beam mode shapes for the above reasons. The use of each type ends with similar results to those discussed in [36]. Then, by eliminating the time derivatives from the equation of motion, we solve for the static deflection of the curved beam as a function of the static voltage to obtain a static equilibrium equation. As a result, we write the static equilibrium as

$$w_s = \sum_{k=1}^{N}\phi_k(x)u_k; \qquad k = 1,\ldots,N \tag{10}$$

where N varies from 1 to any number of modes that are required for the model convergence. Then, substituting this from Equation (10) into Equation (6) and multiplying both sides by $(1 + w_\circ - w_s)^2$, we impose a certain regularization on the response in the vicinity of any present singularity. Then, we multiply the resulting equation by ϕ_j and carry out the integration over ℓ_b in N^{th} algebraic equations, describing the equilibrium position as

$$\begin{aligned}\int_0^1 \phi_j\Big((1 + w_\circ - \sum_{k=1}^{N}\phi_k u_k)^2\Big(\sum_{k=1}^{N}\phi_k^{iv}u_k - \alpha_1(w_\circ'' - \sum_{k=1}^{N}\phi_k''u_k)\int_0^1\Big(2w_\circ'\sum_{k=1}^{N}\phi_k'u_k \\ - (\sum_{k=1}^{N}\phi_k'u_k)^2\Big)dx\Big) + \alpha_2 V_{dc}\Big)dx = 0\end{aligned} \tag{11}$$

A similar procedure to that described above can be also used to simulate the eigenvalues describing the small vibration around the static equilibrium. This is achieved by decomposing the beam deflection into two components: a static w_s and dynamic w_d. Then, substituting these components into Equation (6), dropping the damping coefficients, expanding the electrostatic force around w_d using a Taylor series, dropping the high-order

terms, and retaining only up to the linear term in w_d, we substitute this equation back into the resulting equation.

Similarly, one can write the dynamic component in terms of the Galerkin approximation as

$$w_d = \sum_{k=1}^{N} \phi_k(x) q_i \qquad ; k = 1, \ldots, N \tag{12}$$

By incorporating the mentioned decomposition into the small vibrations problem and substituting ϕ_i^{iv} with $\omega_n^2 \phi_i$, subsequently multiplying the outcome by the mode shapes ϕ_j, and finally conducting the integration along the length of the beam, we obtain a set of N^{th} linear coupled ordinary differential equations that depict the oscillations of the beam around the static equilibrium w under a specific dc voltage.

$$\begin{aligned} &\ddot{q}_j + w_s^{iv} + q_j \omega_n^2 - \alpha_1 \Big(\sum_{k=1}^{N} \phi_i'' q_i \int_0^1 \phi_j \, dx \int_0^1 (2 w_s' w_\circ' - w_s'^2) dx + w_s'' \int_0^1 \phi_j \, dx \int_0^1 2 (w_s' \sum_{k=1}^{N} \phi_i' q_i \\ &- w_\circ' \sum_{k=1}^{N} \phi_i' q_i) dx + w_\circ'' \int_0^1 \phi_j \, dx \int_0^1 2 (w_\circ' \sum_{k=1}^{N} \phi_i' q_i - w_s' \sum_{k=1}^{N} \phi_i' q_i) dx \Big) \\ &= \frac{2 \alpha_2 V_{dc}}{(1 + w_\circ - w_s)^3} \sum_{k=1}^{N} \phi_i' q_i \int_0^1 \phi_j \, dx \end{aligned} \tag{13}$$

where $\quad i = 1, \ldots, N \quad$ and $\quad j = 1, \ldots, N$

Indeed, solving the resulting equation yields the first natural frequencies of the shallow arch microbeam.

3. Results and Discussion

In this section, we analytically examine the variation of static deflection, static profile, and eigenvalues of the shallow arch beam under a dc voltage for various values of initial rise and initial curvature profiles. This step is essential for a more thorough investigation of the fundamental behaviors of a curved beam when subjected to a dc load. It enables better insights into the behavior of the shallow arch and any of its developing phenomena such as snap-through, while altering the initial curvature profile and the maximum initial elevation. Indeed, we plan to examine three different shapes, which include the first symmetric in-plane, the first antisymmetric in-plane, and the second symmetric in-plane modes, as shown in Figure 2.

3.1. Static Behavior vs. dc Voltage

A convergence analysis was conducted in order to ascertain the minimal quantity of modes needed in the Galerkin expansion. This analysis was accomplished by comparing the static deflection achieved from reduced-order models (ROMs) using two to five symmetrical mode shapes; Equation (11). We found that for a shallow arch beam with 3.5 µm mid-point rise, the locations of the bifurcation points named snap-through, snap-back, and pull-in instability vary with the number of modes retained in the Galerkin expansion.

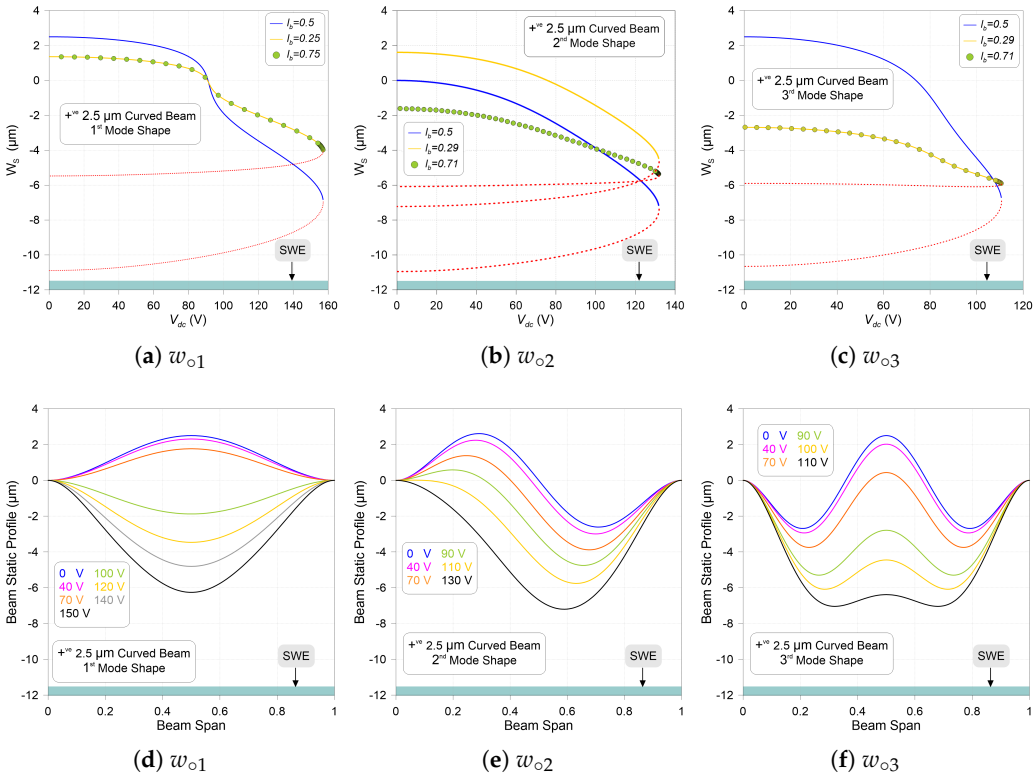
Table 1 presents a comparison of the discrepancies in accuracy observed among the three ROMs at the critical bifurcation points of snap-through, snap-back, and pull-in stability. It is important to highlight that employing an odd number of symmetrical mode shapes results in a more rapid and precise convergence compared to utilizing an even number. Therefore, for the remainder of the analysis, we will adopt the approximation of the five-mode ROM.

Table 1. The relative error of the converge analysis at bifurcation points in terms of voltage compared to those of two-, three-, and five-symmetrical mode approximations.

Modes	ST	ST Error %	SB	SB Error %	PI	PI Error %
2	112.6	0.09	100.2	0	165	7.7
3	113.6	0.8	100.09	0.1	151.99	0.8
5	112.71	–	100.2	–	153.2	–

Here, the maximum static equilibrium position diagrams, which were generated by tracing the static dc voltage parameter, can be examined. The study is centered on examining how the initial curvature's (shape and maximum elevation rise) affects the configuration of the static equilibrium diagram. It's important to highlight that the static results depict the deflection value at a quarter of the beam length for the second mode shape profile, while for the first and third mode shapes, it shows the deflection at the shallow arch mid-point in addition to the quarter of the beam length.

For this purpose, we consider the shallow arch beam illustrated in Figure 1 with dimensions mentioned in Section 2 and initial mid-point rise varying from [2.5–4] µm and increasing with a step size of 0.5 µm. Then, the variation of the microbeam static equilibria as functions of dc voltage were obtained considering two initial curvature profiles ($+^{ve}$ curved-up and $-^{ve}$ curved-down) and three initial profiles, $w_{\circ 1}$, $w_{\circ 2}$, and $w_{\circ 3}$.



(**a**) $w_{\circ 1}$ (**b**) $w_{\circ 2}$ (**c**) $w_{\circ 3}$

(**d**) $w_{\circ 1}$ (**e**) $w_{\circ 2}$ (**f**) $w_{\circ 3}$

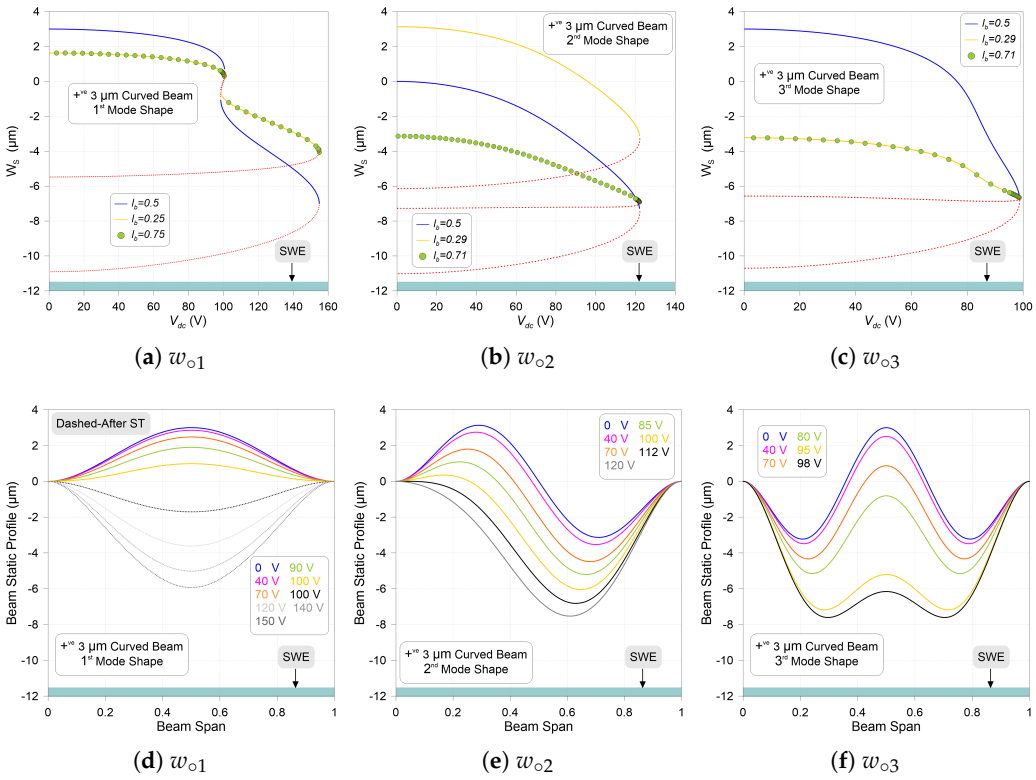
Figure 3. Mid-point and quarter of the beam length deflections as a function of dc voltage obtained for an initial rise of $h_\circ = 2.5$ µm and a curved-up initial profile of (**a**) $w_{\circ 1}$, (**b**) $w_{\circ 2}$, and (**c**) $w_{\circ 3}$. The corresponding static profiles at several dc voltages for each case are shown in (**d**–**f**).

Figure 3 shows the static deflection at mid-point and quarter of the beam length and the static profiles as a function of dc voltage considering a curved-up beam configuration with an initial rise of $h_\circ = 2.5$ µm. Three initial profiles were utilized in this study. The results indicate that only one stable branch of equilibria exists considering the first, second, and third profiles, as shown in Figure 3a–c, respectively. Additionally, it demonstrates that the deflection of the beam increases along a stable solution branch as the dc voltage rises, reaching an unstable solution branch through a saddle-node bifurcation known as 'pull-in'.

We note that the deflections at the off-center points are equal in magnitude for the first profile, Figure 3a, and third profile, Figure 3c, respectively. Nonetheless, this does not hold true for the second profile, as depicted in Figure 3b. The results also show that the maximum deflection occurs at the mid-point for the first and third cases while at the off-center points for the second case. This, in fact, is expected because the second mode has a node located at its span mid-point.

On the other hand, the static bifurcation diagram of the concave-down profile of the shallow arch exhibits behavior analogous to that of the concave-up configuration. Nevertheless, it displays a restricted stable travel range across all scenarios, as illustrated in Figure A1. This limitation arises from the beam's proximity to the stationary electrode (SWE), making it susceptible to voltage-induced destabilization, as detailed in Appendix A.

Alternatively, increasing the initial mid-point rise to $h_\circ = 3$ µm shows that the beam exhibits two stable equilibria considering the first mode shape ($w_{\circ 1}$) profile and a curved-up curvature, as illustrated in Figure 4a. The generated numerical data suggest that the bistability region is relatively restrained and narrow, implying that the shallow arch beam has the capability to transition between states, "jumping down" (snap-through) and reverting to its initial configuration (snap-back) at almost the same identical excitation dc loads. However, the existence of two stable equilibria disappears as the beam's curvature mimics the second ($w_{\circ 2}$) and the third ($w_{\circ 3}$) mode shapes as shown in Figure 4b,c, respectively.



(**a**) $w_{\circ 1}$ (**b**) $w_{\circ 2}$ (**c**) $w_{\circ 3}$

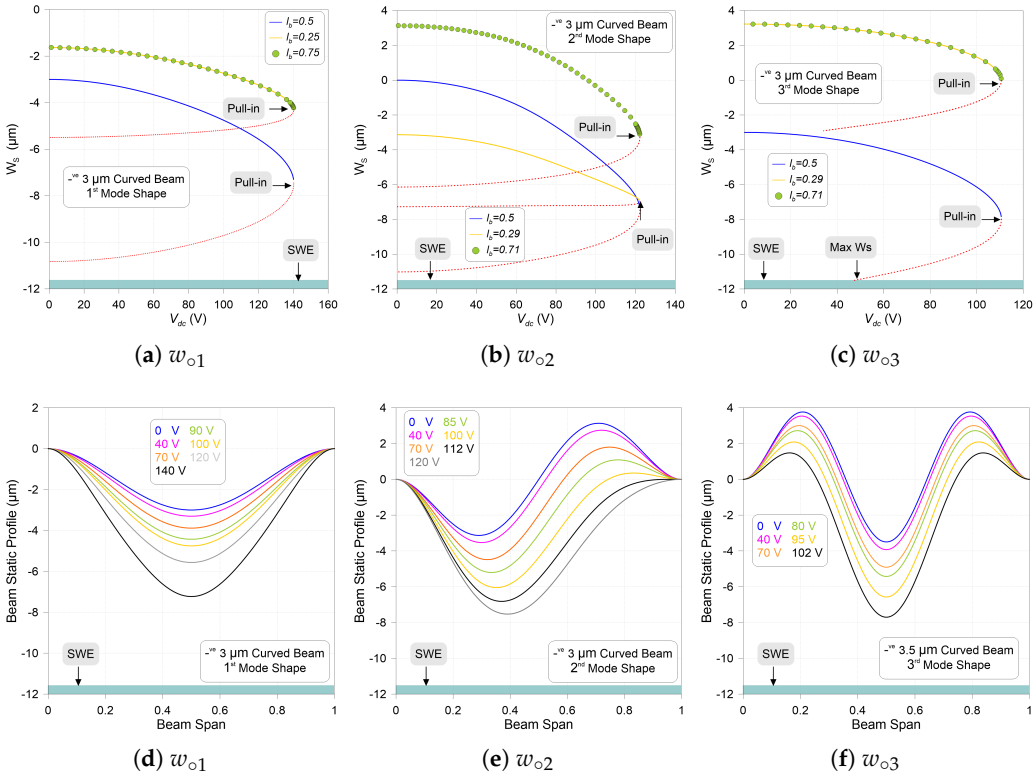
(**d**) $w_{\circ 1}$ (**e**) $w_{\circ 2}$ (**f**) $w_{\circ 3}$

Figure 4. Mid-point and quarter of the beam length deflections as a function of dc voltage obtained for an initial rise of $h_\circ = 3$ µm and a curved-up initial profile of (**a**) $w_{\circ 1}$, (**b**) $w_{\circ 2}$, and (**c**) $w_{\circ 3}$. The corresponding static profiles at several dc voltages for each case are shown in (**d**–**e**).

To further illustrate this phenomenon, we evaluate the corresponding static profile for the first case and subjected to different dc voltages; see Figure 4d. We note that for lower dc load, (>100 V), and for static deflection lower than the initial gap, the beam is deflecting in a standard manner of an elastic beam and around a single equilibrium. Once its mid-point deflection reaches the central line, the beam profile jumps to the counter configuration, characterized by a snap-through (ST), with mid-point deflection increasing as dc voltage increases. The profiles corresponding to the counter-curvature are marked as dashed lines

in Figure 4d. However, as depicted in the same figure, this phenomenon does not hold when the beam emulates the second and third shapes.

It is important to mention that the nodes of the second and third modes are disappearing as the voltage reaches the pull-in value, illustrated in Figure 4e,f. Alternatively, the static bifurcation diagrams when the beam is curved-down are shown in Figure 5. We note that only a single stable equilibrium exists for all three cases because the beam is set closer to the stationary electrode.



(**a**) $w_{\circ 1}$ (**b**) $w_{\circ 2}$ (**c**) $w_{\circ 3}$

(**d**) $w_{\circ 1}$ (**e**) $w_{\circ 2}$ (**f**) $w_{\circ 3}$

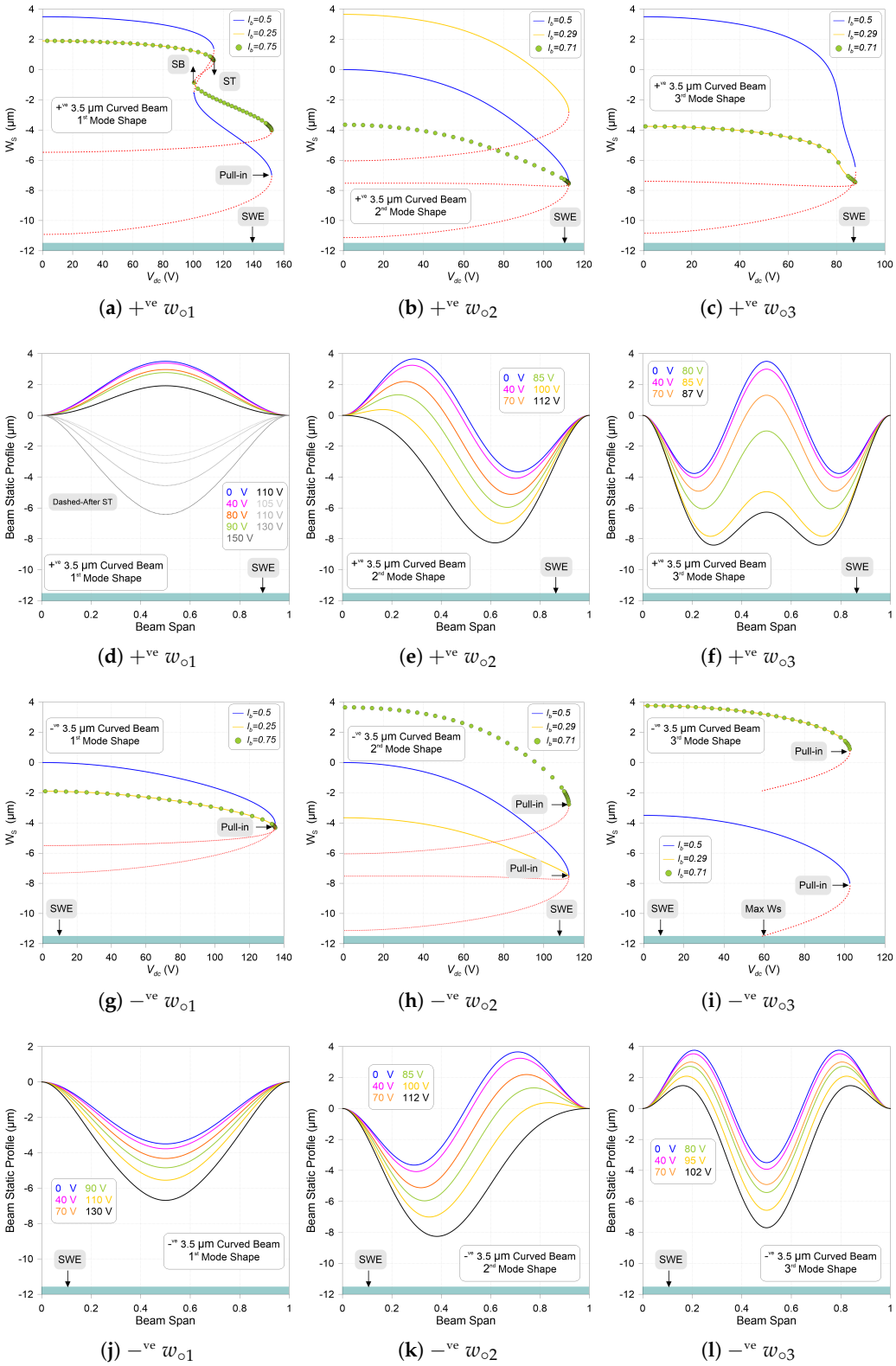
Figure 5. Mid-point and quarter of the beam length deflections as a function of dc voltage obtained for an initial rise of $h_\circ = 3$ µm and a curved-down initial profile of (**a**) $w_{\circ 1}$, (**b**) $w_{\circ 2}$, and (**c**) $w_{\circ 3}$. The corresponding static profiles at several dc voltages for each case are shown in (**d**–**f**).

Figures 6a–c and 7a–c, respectively, depict the bifurcation diagrams of the beam static deflection including both stable and unstable branches as a function of dc voltages. The beam initial mid-point is set to $h_\circ = 3.5$ µm for the first case and $h_\circ = 4$ µm for the second case. These diagrams take into account three distinct initial curvature profiles: the first, second, and third natural mode shapes of a doubly-clamped beam similar to those obtained above. In this analysis, the deflections are simulated at the mid-point and quarter node positions of each respective initial curvature shape. This is conducted to investigate the effect of a higher initial rise on the static response of the shallow arch beam such that its curvature mimics the first three mode shapes of the clamped–clamped beam.

Furthermore, when the shallow arch is concave-up, Figures 6 and 7a–c, as compared to that where the arch is concave-down, Figures 6 and 7g–i, the beam exhibits two stable equilibria when considering the shallow arch mimicking the concave-up first mode-shape-like arrangement. This bistability refers to the existence of two stable equilibrium positions at the same presumed dc voltage resulting in a hysteric band delimited by the snap-through (ST) and snap-back (SB) nodes, both shown in Figures 6a and 7a, respectively.

In this particular case, the arch experiences snap-through followed by pull-in as the applied dc voltage increases. However, for all other cases, the microarch undergoes immediate pull-in. Indeed, when the beam presumes an initial curvature corresponding to the second and third mode shapes of a clamped–clamped beam, only a single bistability

behavior is recorded for various dc voltage; see Figure 6b,c for the first case and Figure 7b,c for the second case.



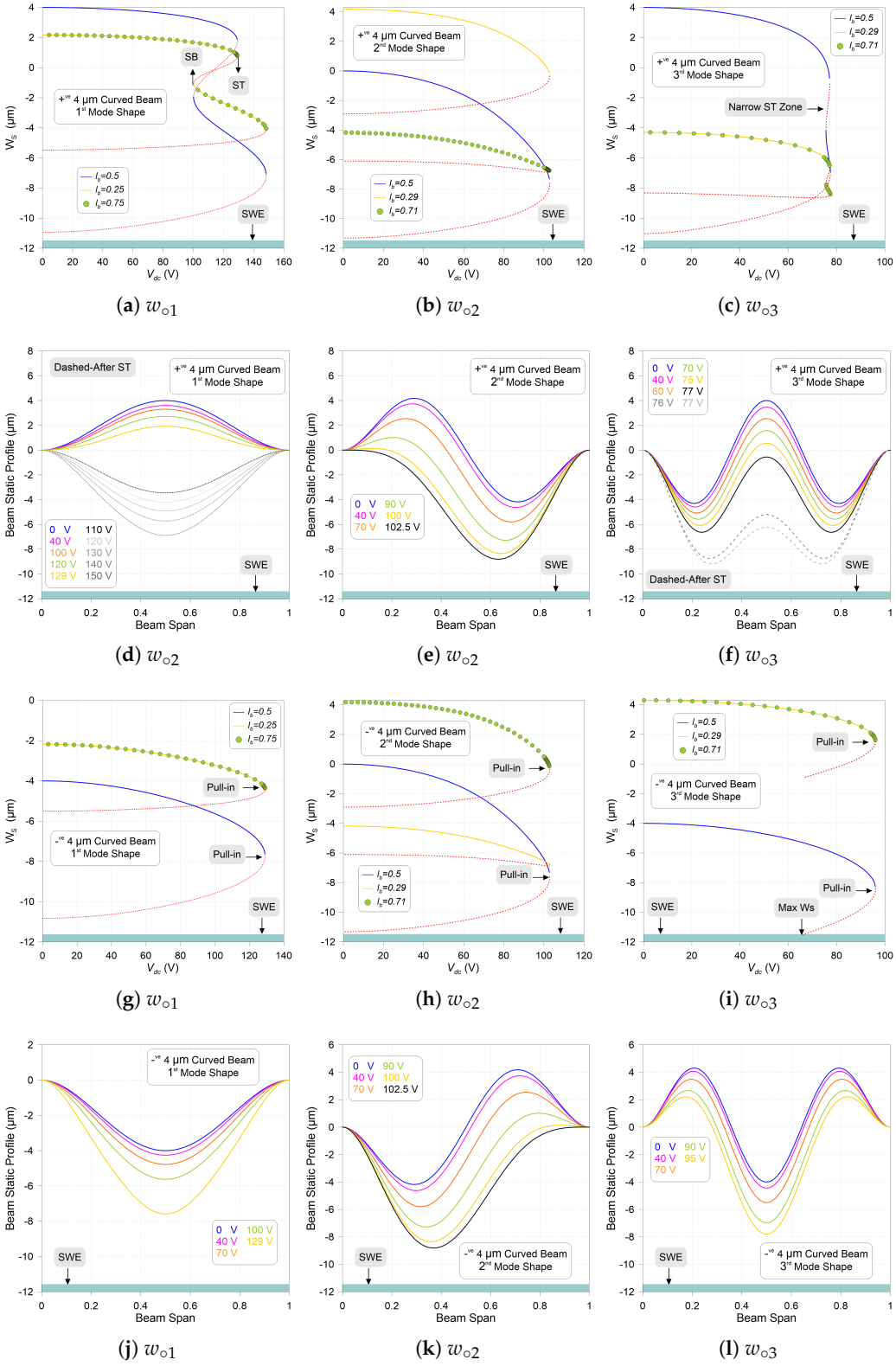
(**a**) $+^{ve}\ w_{\circ 1}$ (**b**) $+^{ve}\ w_{\circ 2}$ (**c**) $+^{ve}\ w_{\circ 3}$

(**d**) $+^{ve}\ w_{\circ 1}$ (**e**) $+^{ve}\ w_{\circ 2}$ (**f**) $+^{ve}\ w_{\circ 3}$

(**g**) $-^{ve}\ w_{\circ 1}$ (**h**) $-^{ve}\ w_{\circ 2}$ (**i**) $-^{ve}\ w_{\circ 3}$

(**j**) $-^{ve}\ w_{\circ 1}$ (**k**) $-^{ve}\ w_{\circ 2}$ (**l**) $-^{ve}\ w_{\circ 3}$

Figure 6. Mid-point and quarter of the beam length deflections as a function of dc voltage obtained for an initial rise of $h_\circ = 3.5$ μm and a curved-up initial profile of (**a**) $w_{\circ 1}$, (**b**) $w_{\circ 2}$, and (**c**) $w_{\circ 3}$. The corresponding static profiles at several dc voltages for each case are shown in (**d**,**e**).



(**a**) $w_{\circ 1}$ (**b**) $w_{\circ 2}$ (**c**) $w_{\circ 3}$

(**d**) $w_{\circ 2}$ (**e**) $w_{\circ 2}$ (**f**) $w_{\circ 3}$

(**g**) $w_{\circ 1}$ (**h**) $w_{\circ 2}$ (**i**) $w_{\circ 3}$

(**j**) $w_{\circ 1}$ (**k**) $w_{\circ 2}$ (**l**) $w_{\circ 3}$

Figure 7. Mid-point and quarter of the beam length deflections as a function of dc voltage obtained for an initial rise of $h_\circ = 4$ μm and a curved-up initial profile of (**a**) $w_{\circ 1}$, (**b**) $w_{\circ 2}$, and (**c**) $w_{\circ 3}$. The corresponding static profiles at several dc voltages for each case are shown in (**d**–**f**).

Figures 6 and 7d–f display the static profiles of the shallow arch with curved-up curvature excited by various dc voltages. They are describing consistent symmetry without

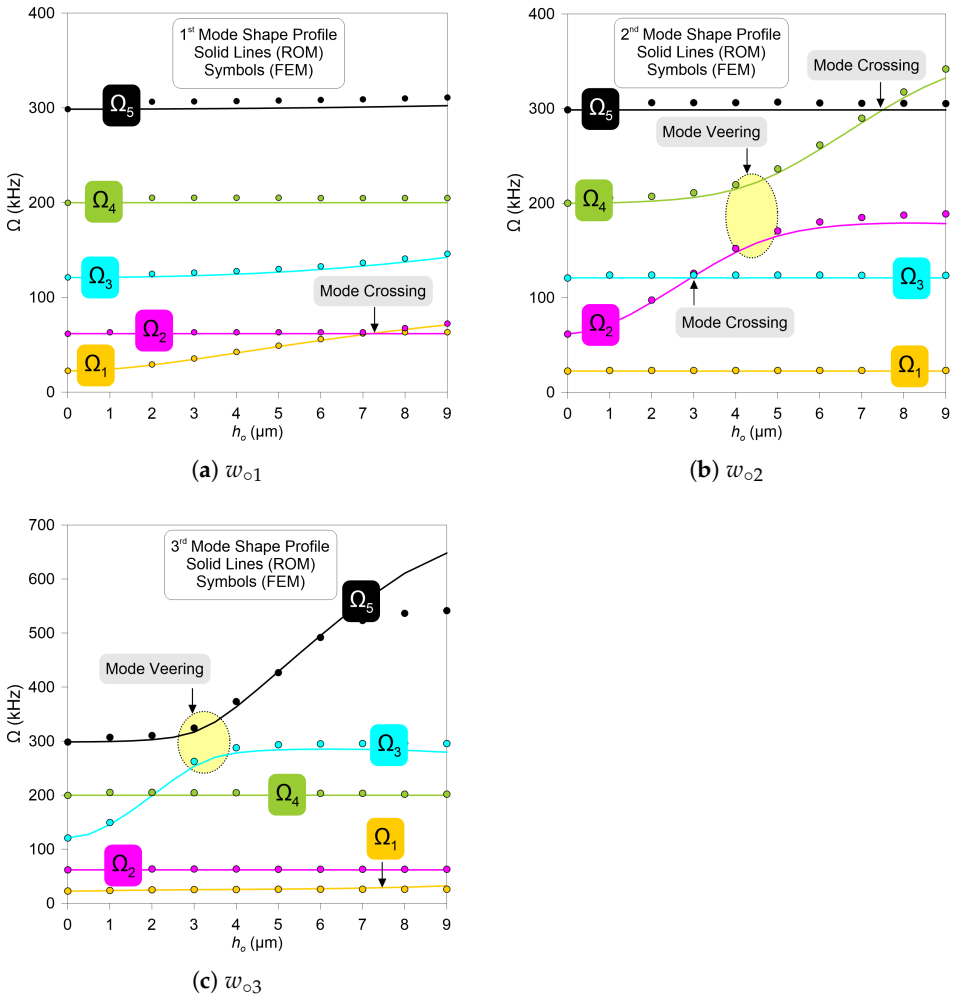
notable options of symmetry-breaking behavior. This means that the beam maintains its symmetric (first and third) and asymmetric (second) shapes.

It is worth noting that in the third-mode-like shape case, the simulated figures indicate a trend in which the stroke decreases, while the pull-in voltage increases, when considering both concave-up and concave-down profiles. This trend suggests that the effective stiffness of the shallow arch increases with the clamped–clamped shallow arch stretching while considering it concave-down.

With an increase in the assumed maximum rise amplitude to 4 µm, there is a noticeable enhancement of the bistable behavior accompanied by a broader hysteresis band in the concave-up first mode shape arrangement, as illustrated in Figure 7a. Furthermore, the third mode shape, as depicted in Figure 7c, also begins to demonstrate bistable behavior under these conditions, while the second mode remains unaffected by the initial rise value, as shown in Figure 7b. Nothing can be highlighted when considering the concave-down arrangement of Figure 7d–f as compared to the previous case.

3.2. Eigenvalues vs. dc Voltage

In this section, we evaluate the variation of the natural frequencies of the shallow arch with various initial rise levels, three initial profiles, and under several dc voltages. Toward this, we substitute the static deflections obtained above for each case in Equation (13) and then solve for the corresponding eigenvalues. Figure 8 shows the first five natural frequencies versus the initial rise considering the first mode ($w_{\circ 1}$), second mode ($w_{\circ 2}$), and third mode ($w_{\circ 3}$) profiles obtained using five-modes ROM and FEM, respectively.



(**a**) $w_{\circ 1}$ (**b**) $w_{\circ 2}$

(**c**) $w_{\circ 3}$

Figure 8. Variation of the first five natural frequencies Ω_i as a function of the initial rise $h_\circ$ and a curved-up initial profile mimics (**a**) first mode $w_{\circ 1}$, (**b**) second mode $w_{\circ 2}$, and (**c**) third mode $w_{\circ 3}$.

The FEM software COMSOL Multiphysics (5.3a) [37] was also employed to solve for the variation of the eigenfrequencies as a function of the static voltage for all cases. A three-dimensional model was generated following the sensor's dimensions. The beam is fixed at its two ends. Tetrahedral elements were employed to mesh the 3D model with number of elements approximately reached (35 K). The elements size ranges from 10 to 70 µm. The Solid Mechanics Interface module was utilized to solve for the variation of the first five eigenfrequencies with the beam profile and mid-point rise change.

The results obtained using the developed ROM are shown in solid lines while those obtained using the FEM model are marked with symbols. As seen in Figure 8a, there is a crossing between the frequency corresponding to the first symmetric Ω_1, marked as a dark yellow line (—), and the frequency corresponding to the first antisymmetric Ω_2, marked as a dark magenta line (—) that occurs at $h_\circ = 7.5$ µm. We note that other frequencies do not cross nor veer.

On the other hand, for shallow arch mimicking the concave-up second mode-shape-like arrangement, several crossings between the odd and even eigenfrequencies were triggered, as shown in Figure 8b. The first crossing occurs between the first antisymmetric Ω_2 and the frequency corresponding to the second symmetric Ω_3, marked as a light blue line (—), at $h_\circ = 3$ µm.

Another mode transition is observed between the second antisymmetric mode Ω_4 (indicated by the green line —) and the frequency associated with the third symmetric mode Ω_5 (indicated by the black line —). However, this transition occurs at a higher initial rise. Here, it should be emphasized that the eigenvalues corresponding to the symmetric modes remain unaltered when the beam curvature imitates the second mode shape of a clamped–clamped beam.

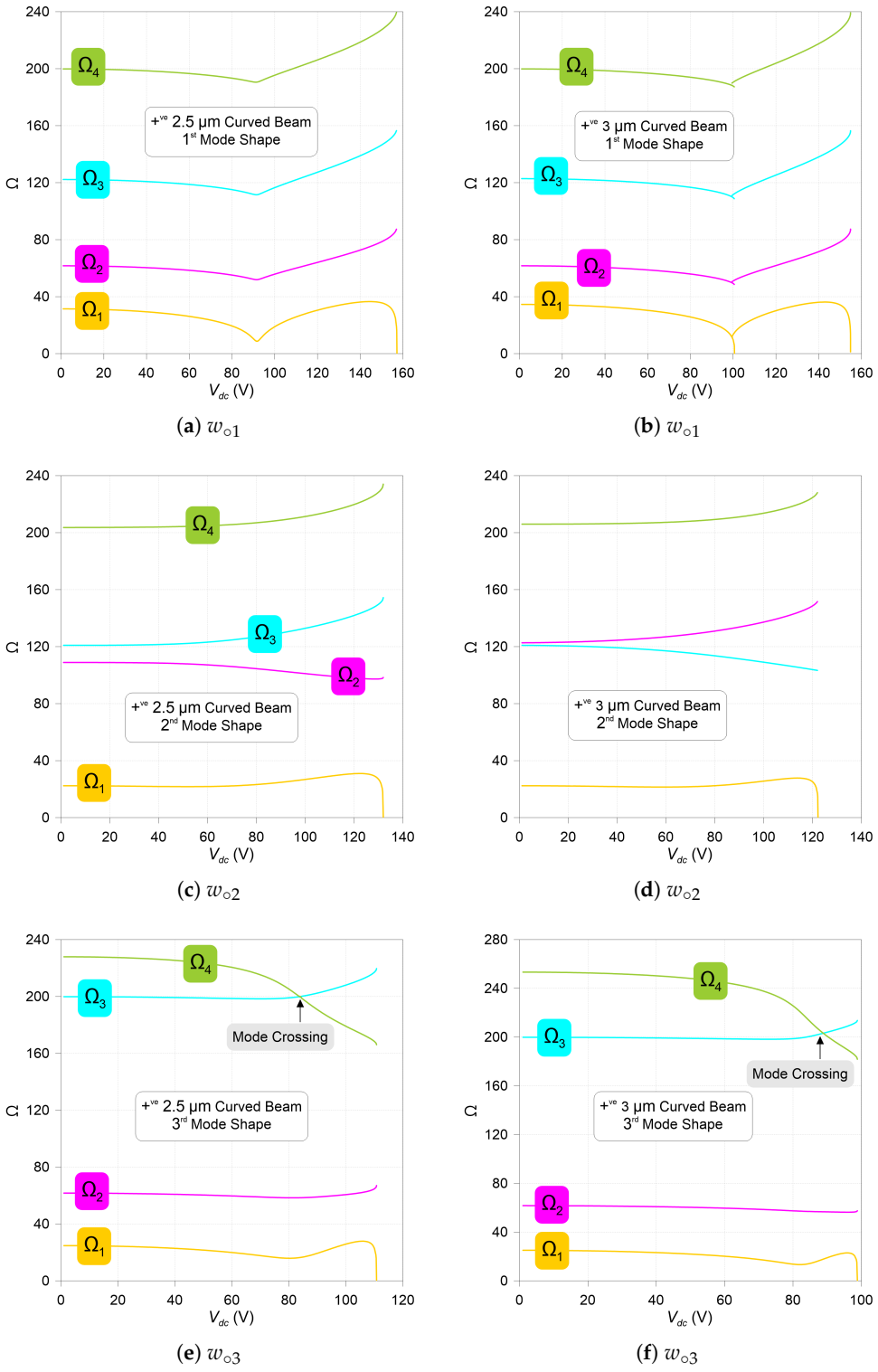
Furthermore, when we initially configured the shallow arch with a third-mode-like shape, the eigenvalues began to demonstrate distinct mode-veering and -crossing behaviors. The mode-veering and mode-crossover occurrences are controlled by intricate underlying mechanisms originating from the interaction of material characteristics, boundary conditions, and structural dynamics. When distinct vibration modes' resonance frequencies move too close to one another, a nonlinear interaction between them happens. On the contrary, mode-crossing happens when two or more modes cross paths in frequency space, which results in an abrupt alteration of the resonator's dominant vibrational behavior. These phenomena are clearly a consequence of nonlinearity present in specific parameters within the equations of motion, which inevitably lead to these mode interactions. It is important to mention that the third frequency Ω_3 increases drastically as the initial rise increases until it crosses the second antisymmetric, as illustrated in Figure 8c. A good agreement between both models was achieved, expect for higher initial rise and a shallow arch with a third-mode-like shape. Following that, the eigenvalue consistently increases until it approaches the fifth frequency, at which both modes undergo a mode-veering process.

Indeed, if the initial arrangement of a shallow arch beam closely resembles a mode shape that is symmetrical, the eigenvalues that are antisymmetric remain constant because the position of the central node remains unchanged. Similarly, when the initial shape of the arch beam resembles a mode that is antisymmetric, the eigenvalues that are symmetrical do not change since the positions of the interior nodes remain unaltered.

Subsequently, we examined the effect of a static voltage on the fundamental frequencies of the beam, considering various mid-point elevations and initial profiles. To achieve this, we replaced the previously obtained static equilibrium with a reduced-order model (ROM) featuring three symmetric and two antisymmetric modes. We then solved the coupled linear eigenvalue problem to determine the corresponding eigenvalues under the influence of a static dc load.

The first four fundamental frequencies were computed using the ROM and they correspond to the first and second in-plane symmetric and antisymmetric mode, respectively. Figure 9a,c,e show the variation of the resonance frequencies as a function of dc voltage considering a curved-up beam configuration with an initial rise of $h_\circ = 2.5$ µm and three

initial profiles. Considering the first profile ($w_{\circ 1}$)-like arrangement, we found that the beam initial rise was not sufficient enough to activate the snap-through, although it showed a peak at 90 V. In addition,, the eigenvalues did not show any sign of snap-through behavior for a beam curvature mimicking the second profile, as illustrated in Figure 9c.



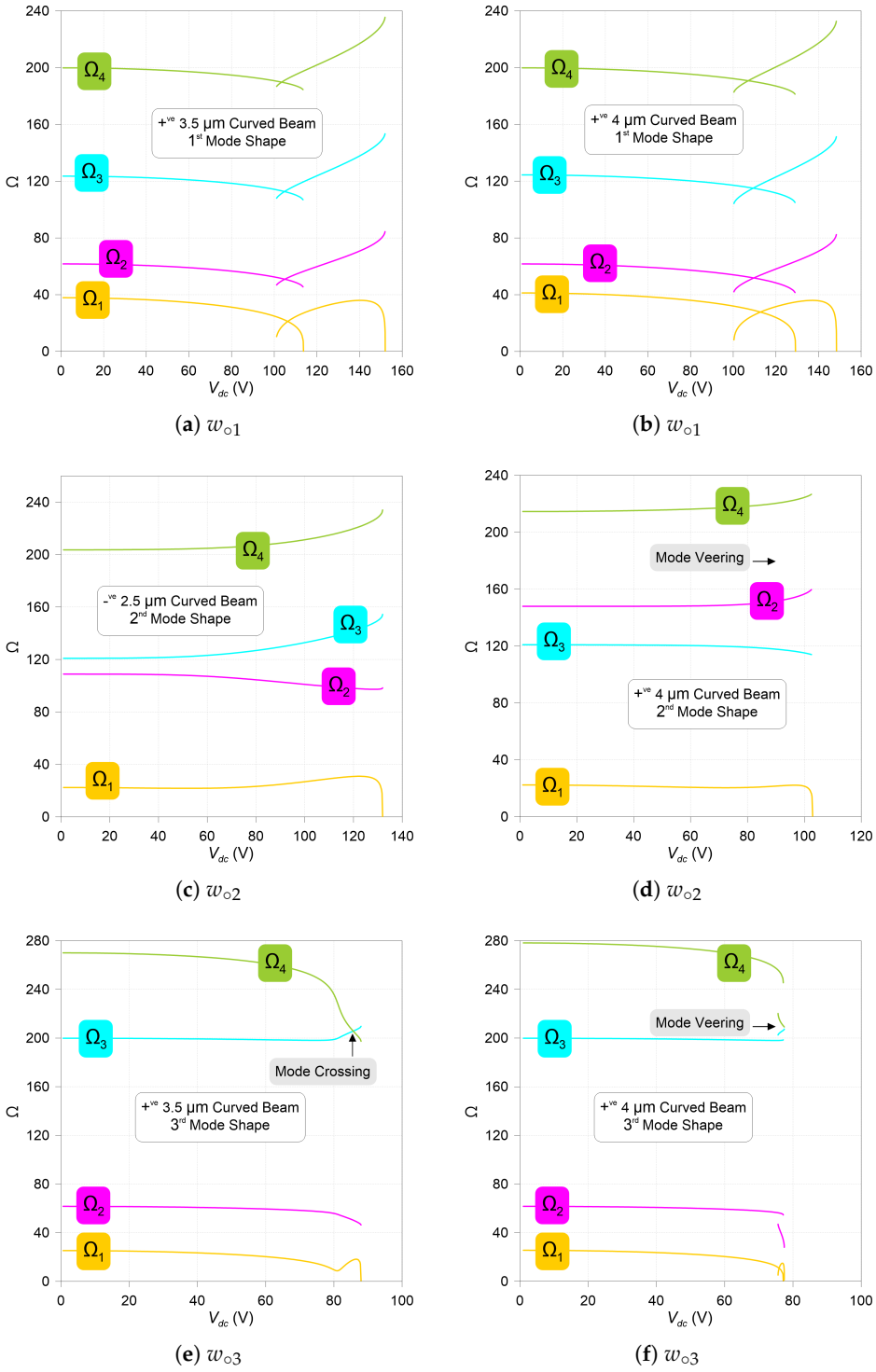
(**a**) $w_{\circ 1}$ (**b**) $w_{\circ 1}$

(**c**) $w_{\circ 2}$ (**d**) $w_{\circ 2}$

(**e**) $w_{\circ 3}$ (**f**) $w_{\circ 3}$

Figure 9. The variation of the fundamental frequencies of the beam as a function of the dc voltage for a mid-point initial rise of $h_{\circ} = 2.5$ μm and a curved-up initial profile of (**a**) $w_{\circ 1}$, (**c**) $w_{\circ 2}$, and (**e**) $w_{\circ 3}$ and $h_{\circ} = 3$ μm, and a curved-up initial profile of (**b**) $w_{\circ 1}$, (**d**) $w_{\circ 2}$, and (**f**) $w_{\circ 3}$.

On the other hand, we note that for a beam-curvature-like third-mode profile arrangement, the first and second resonance frequencies (Ω_1 and Ω_2) decrease as the voltage increases. However, this is not the case for the third and fourth frequencies. The results show that the third frequency Ω_3, marked as a sky blue line (—), increases as the dc voltage increases until it crosses the fourth frequency Ω_4, marked as a green line (—), at 84 V, as shown in Figure 9e.



(**a**) $w_{\circ 1}$ (**b**) $w_{\circ 1}$

(**c**) $w_{\circ 2}$ (**d**) $w_{\circ 2}$

(**e**) $w_{\circ 3}$ (**f**) $w_{\circ 3}$

Figure 10. The variation of the fundamental frequencies of the beam as a function of the dc voltage for a mid-point initial rise of $h_\circ = 3.5$ μm and a curved-up initial profile of (**a**) $w_{\circ 1}$, (**c**) $w_{\circ 2}$, (**e**) $w_{\circ 3}$, and $h_\circ = 4$ μm, and a curved-up initial profile of (**b**) $w_{\circ 1}$, (**d**) $w_{\circ 2}$, and (**f**) $w_{\circ 3}$.

Alternatively, increasing the mid-point rise to $h_\circ = 3$ µm shows a possibility for the snap-through phenomenon as long as the beam curvature mimics the first profile, as shown in Figure 9b. The figure indicates a relatively restrained and narrow snap-through band. This, in fact, is consistent with the static bifurcation diagram in Figure 4a.

We note that the third frequency is lower than the second frequency as the beam curvature follows the second mode profile $w_{\circ 2}$. These two values are moving away from each other as the dc voltage increases, as shown in Figure 9d. This is a classical behavior of veering phenomenon. On the other hand, a mode-crossing phenomenon is observed between the third and fourth frequencies when the shallow arch initial profile transitions to the third mode like shape, as depicted in Figure 9d.

Similar nonlinear phenomena were also observed for the beam with mid-point rise of $h_\circ = 3.5$ µm and $h_\circ = 4$ µm, respectively. Nevertheless, it's worth noting that the extent of the snap-through instability grows as the mid-point elevation increases, and the curvature aligns with a shape resembling the first mode, as illustrated in Figure Figure 10a for the first initial rise and Figure 10b for the second initial rise. Furthermore, an instantaneous snap-through event, characterized by a narrow dc voltages band, occurs when the mid-point rise is 4 µm, and mode-veering becomes evident as the curvature of the beam closely resembles the third mode shape, as depicted in Figure 10f. Appendix A provides a comprehensive presentation of the fundamental frequency fluctuations of the beam with the dc voltage, and for initial profiles characterized by a downward curvature, ensuring a comprehensive analysis.

It is important to acknowledge that the shallow arched MEMS resonators are highly sensitive to various parameters, such as residual stresses, geometric imperfections, and material characteristics. Material qualities like Young's modulus, density, and Poisson's ratio can significantly influence the mechanical behavior of the resonator under different loading conditions. Alterations in these properties can lead to changes in the overall performance, damping behavior, and resonant frequency of the device. Moreover, the residual stresses present in the fabricated structure can modify its mechanical response and affect metrics like stiffness, mode shapes, and stability [38,39]. These stresses, induced by factors like thermal fluctuations or the manufacturing process, need to be carefully considered in the design and optimization phase to mitigate any adverse effects on the resonator's functionality. Additionally, the performance of shallow arched MEMS resonators is strongly impacted by geometric irregularities.

Moreover, the behavior of shallow arched MEMS resonators is significantly influenced by geometric imperfections. Anomalies in performance may arise due to deviations such as surface roughness, dimensional variations, and errors in fabrication, introducing asymmetries and irregularities into the system. These imperfections can not only affect the overall functioning and reliability of the device but also influence mode shapes, energy dissipation mechanisms, and resonance frequencies. It is essential to optimize the design and operation of shallow arched MEMS resonators for a variety of applications in the fields of sensing, signal processing, and communication systems. This optimization process requires a thorough understanding and assessment of the effects of material characteristics, residual stresses, and geometric irregularities.

4. Conclusions

This study involved a comprehensive exploration of the nonlinear characteristics in both the static behavior and the variations of the linearized eigenvalue problem for an initially curved microbeam with a profile mimicking the first in-plane symmetric and antisymmetric and the second symmetric mode shapes. We proposed and investigated a mathematical model for such an innovative mode-localized sensor/actuator that incorporates a single sensitive shallow arch flexible microbeam element. This model accounts for the effect of energy exchange among various vibration modes, offering significant potential for applications in high-precision sensing. Indeed, we examined the influence of the initial shape arrangement of the shallow arch microbeam. The simulated data revealed that,

through a well-designed configuration of the initial shape of the flexible electrode and precise adjustment of the maximum initial rise and the actuating dc load, the transition to specific bistable static displacements at desired levels was achieved, enhancing the potential utility of such a system as a high-stroke actuator. The results also showed that, in the case of a microbeam with a third-mode-like symmetric initial curvature, regions of mode-veering emerge, indicating a coupling between the concerned symmetric and asymmetric vibration modes. The analysis reveals that it is advised to carefully choose materials with good mechanical stability and electrical conductivity when manufacturing electrostatically actuated initially curved beams assuming multimodal initial curvature profiles. To sum up, this research offers insights to enhance the design and functionality of MEMS devices for improved functionality and reliability.

Author Contributions: Conceptualization, methodology, visualization, validation, and draft writing: A.M.A. and H.M.O.; manuscript revision and supervision: A.M.A. and H.M.O. All authors have read and agreed to the published version of the manuscript.

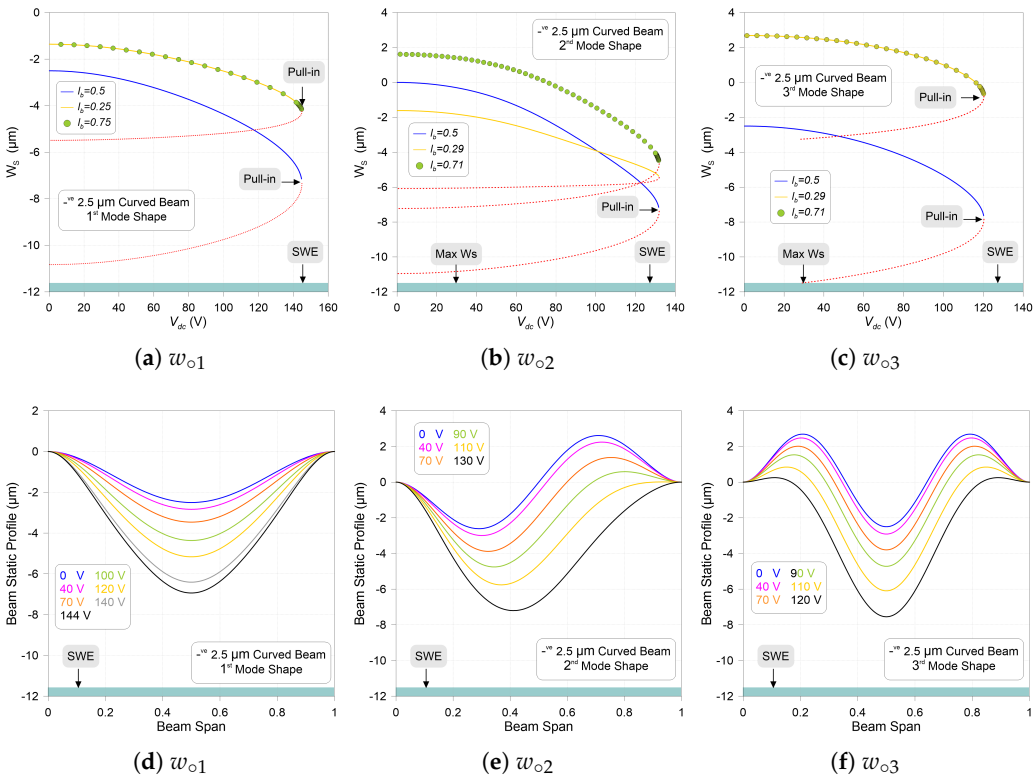
Funding: The author extends appreciation to the Deputyship for Research & Innovation, Ministry of Education in Saudi Arabia, for funding this research work through the project number ISP23-54.

Data Availability Statement: All data were included in this study. Data sharing is not applicable to this article.

Acknowledgments: The author extends appreciation to the Deputyship for Research & Innovation, Ministry of Education in Saudi Arabia, for funding this research work through the project number ISP23-54. The second author acknowledges the support provided by the MedTech at the South Mediterranean University, Lac2, Tunis.

Conflicts of Interest: The authors declare no conflicts of interest.

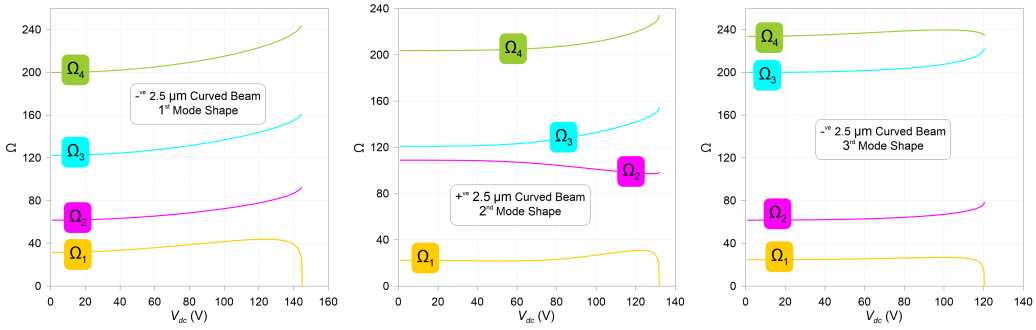
Appendix A



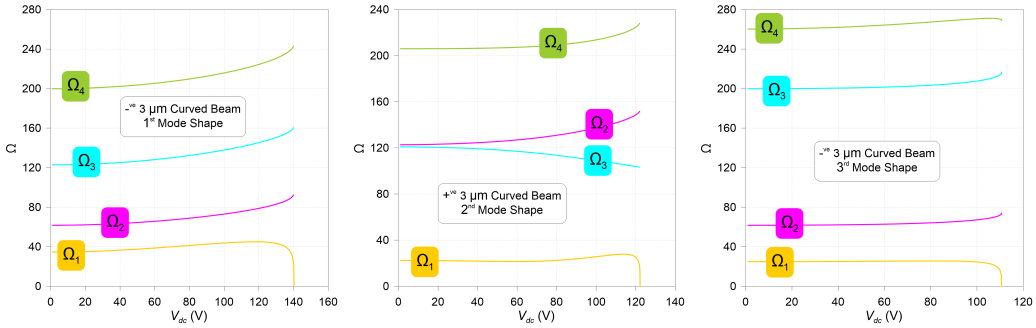
(**a**) $w_{\circ 1}$ (**b**) $w_{\circ 2}$ (**c**) $w_{\circ 3}$

(**d**) $w_{\circ 1}$ (**e**) $w_{\circ 2}$ (**f**) $w_{\circ 3}$

Figure A1. Mid-point and quarter of the beam length deflections as a function of dc voltage obtained for an initial rise of $h_\circ = 2.5$ µm and a curved-down initial profile of (**a**) $w_{\circ 1}$, (**b**) $w_{\circ 2}$, and (**c**) $w_{\circ 3}$. The corresponding static profiles at several dc voltages for each case are shown in (**d**–**f**).

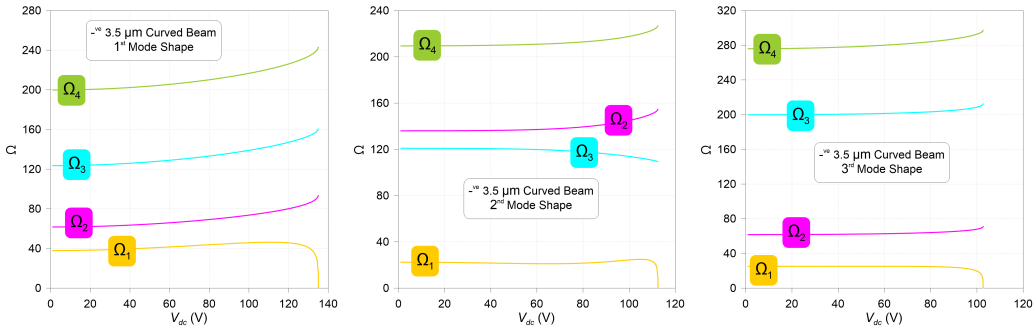


(**a**) $w_{\circ 1}$ (**b**) $w_{\circ 2}$ (**c**) $w_{\circ 3}$

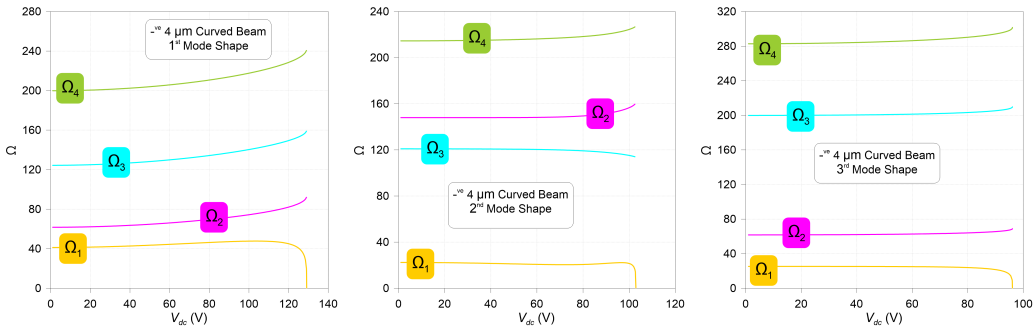


(**d**) $w_{\circ 1}$ (**e**) $w_{\circ 2}$ (**f**) $w_{\circ 3}$

Figure A2. The variation of the fundamental frequencies of the beam as a function of the dc voltage for a mid-point initial rise of $h_\circ = 2.5$ μm and a curved-down initial profile of (**a**) $w_{\circ 1}$, (**b**) $w_{\circ 2}$, (**c**) $w_{\circ 3}$, and $h_\circ = 3$ μm, and a curved-up initial profile of (**d**) $w_{\circ 1}$, (e) $w_{\circ 2}$, and (**f**) $w_{\circ 3}$.



(**a**) $w_{\circ 1}$ (**b**) $w_{\circ 2}$ (**c**) $w_{\circ 3}$



(**d**) $w_{\circ 1}$ (**e**) $w_{\circ 2}$ (**f**) $w_{\circ 3}$

Figure A3. The variation of the fundamental frequencies of the beam as a function of the dc voltage for a mid-point initial rise of $h_\circ = 3.5$ μm and a curved-down initial profile of (**a**) $w_{\circ 1}$, (**b**) $w_{\circ 2}$, (**c**) $w_{\circ 3}$, and $h_\circ = 4$ μm, and a curved-up initial profile of (**d**) $w_{\circ 1}$, (**e**) $w_{\circ 2}$, and (**f**) $w_{\circ 3}$.

References

1. Younis, M.I. *MEMS Linear and Nonlinear Statics and Dynamics*; Springer Science & Business Media: Berlin/Heidelberg, Germany, 2011; Volume 20.
2. Haronian, D. A low-cost micromechanical accelerometer with integrated solid-state sensor. *Sens. Actuators A Phys.* **2000**, *84*, 149–155. [CrossRef]
3. Morozov, N.F.; Indeitsev, D.A.; Igumnova, V.S.; Lukin, A.V.; Popov, I.A.; Shtukin, L.V. Nonlinear dynamics of mode-localized MEMS accelerometer with two electrostatically coupled microbeam sensing elements. *Int. J.-Non-Linear Mech.* **2022**, *138*, 103852.
4. Pachkawade, V. State-of-the-art in mode-localized MEMS coupled resonant sensors: A comprehensive review. *IEEE Sens. J.* **2021**, *21*, 8751–8779. [CrossRef]
5. Benjamin, E.; Lulinsky, S.; Krylov, S. Design and implementation of a bistable force/acceleration sensing device considering fabrication tolerances. *J. Microelectromech. Syst.* **2018**, *27*, 854–865. [CrossRef]
6. Krakover, N.; Ilic, B.R.; Krylov, S. Displacement sensing based on resonant frequency monitoring of electrostatically actuated curved micro beams. *J. Micromech. Microeng.* **2016**, *26*, 115006. [CrossRef] [PubMed]
7. Kessler, Y.; Liberzon, A.; Krylov, S. Flow velocity gradient sensing using a single curved bistable microbeam. *J. Microelectromech. Syst.* **2020**, *29*, 1020–1025. [CrossRef]
8. Tang, X.; Liu, F. A novel benzene quantitative analysis method using miniaturized metal ionization gas sensor and non-linear bistable dynamic system. *Bioengineered* **2015**, *6*, 294–296. [CrossRef]
9. Ouakad, H.M.; Alneamy, A.M. Static and Eigenvalue Analysis of Electrostatically Coupled and Tunable Shallow Micro-Arches for Sensing-Based Applications. *Micromachines* **2023**, *14*, 903. [CrossRef]
10. Alneamy, A.M.; Ouakad, H.M. Inertia mass bio-sensors based on snap-through phenomena in electrostatic MEMS shallow arch resonators. *Int. J. Mech. Sci.* **2023**, *238*, 107825. [CrossRef]
11. Tella, S.A.; Younis, M.I. Toward cascadable MEMS logic device based on mode localization. *Sens. Actuators A Phys.* **2020**, *315*, 112367. [CrossRef]
12. Medina, L. Unified dynamic bistability criteria in electrostatically actuated curved prestressed microbeams. *Int. J. Mech. Sci.* **2024**, *263*, 108765. [CrossRef]
13. Mesbah, A.; Belabed, Z.; Tounsi, A.; Ghazwani, M.H.; Alnujaie, A.; Aldosari, S.M. Assessment of New Quasi-3D Finite Element Model for Free Vibration and Stability Behaviors of Thick Functionally Graded Beams. *J. Vib. Eng. Technol.* **2023**, *12*, 2231–2247. [CrossRef]
14. Vlajic, N.; Fitzgerald, T.; Nguyen, V.; Balachandran, B. Geometrically exact planar beams with initial pre-stress and large curvature: Static configurations, natural frequencies, and mode shapes. *Int. J. Solids Struct.* **2014**, *51*, 3361–3371. [CrossRef]
15. Zhou, Y.; Yi, Z.; Stanciulescu, I. Nonlinear buckling and postbuckling of shallow arches with vertical elastic supports. *J. Appl. Mech.* **2019**, *86*, 061001. [CrossRef]
16. Nicoletti, R. On the natural frequencies of simply supported beams curved in mode shapes. *J. Sound Vib.* **2020**, *485*, 115597. [CrossRef]
17. Karaagac, C.; Ozturk, H.; Sabuncu, M. Crack effects on the in-plane static and dynamic stabilities of a curved beam with an edge crack. *J. Sound Vib.* **2011**, *330*, 1718–1736. [CrossRef]
18. Eisenberger, M.; Efraim, E. In-plane vibrations of shear deformable curved beams. *Int. J. Numer. Methods Eng.* **2001**, *52*, 1221–1234. [CrossRef]
19. Yang, F.; Sedaghati, R.; Esmailzadeh, E. Free in-plane vibration of general curved beams using finite element method. *J. Sound Vib.* **2008**, *318*, 850–867. [CrossRef]
20. Mohamed, S.A.; Assie, A.E.; Eltaher, M.A. Novel incremental procedure in solving nonlinear static response of 2D-FG porous plates. *THin-Walled Struct.* **2023**, *189*, 110779. [CrossRef]
21. Medina, L.; Gilat, R.; Krylov, S. Symmetry breaking in an initially curved pre-stressed micro beam loaded by a distributed electrostatic force. *Int. J. Solids Struct.* **2014**, *51*, 2047–2061. [CrossRef]
22. Alnujaie, A.; Akbas, S.D.; Eltaher, M.A.; Assie, A. Forced vibration of a functionally graded porous beam resting on viscoelastic foundation. *Geomech. Eng.* **2021**, *24*, 91–103.
23. Sharma, A.K.; Godara, R.; Joglekar, M.M. Static and DC dynamic pull-in analysis of curled microcantilevers with a compliant support. *Microsyst. Technol.* **2019**, *25*, 965–975. [CrossRef]
24. Medina, L.; Gilat, R.; Krylov, S. Latching in bistable electrostatically actuated curved micro beams. *Int. J. Eng. Sci.* **2017**, *110*, 15–34. [CrossRef]
25. Shojaeian, M.; Beni, Y.T.; Ataei, H. Size-dependent snap-through and pull-in instabilities of initially curved pre-stressed electrostatic nano-bridges. *J. Phys. D Appl. Phys.* **2016**, *49*, 295303. [CrossRef]
26. Alcheikh, N.; Ouakad, H.M.; Mbarek, S.B.; Younis, M.I. Crossover/veering in V-shaped MEMS resonators. *J. Microelectromech. Syst.* **2021**, *31*, 74–86. [CrossRef]
27. Rosenberg, S.; Shoshani, O. Zero-dispersion point in curved micro-mechanical beams. *Nonlinear Dyn.* **2022**, *107*, 1–14. [CrossRef]
28. Alneamy, A.; Khater, M.; Al-Ghamdi, M.; Abdel-Aziz, A.; Heppler, G.; Abdel-Rahman, E. Large oscillation of electrostatically actuated curved beams. *J. Micromech. Microeng.* **2020**, *30*, 095005. [CrossRef]
29. Alfosail, F.K.; Hajjaj, A.Z.; Younis, M.I. Theoretical and experimental investigation of two-to-one internal resonance in MEMS arch resonators. *J. Comput. Nonlinear Dyn.* **2019**, *14*, 011001. [CrossRef]

30. Ghayesh, M.H.; Farokhi, H. Bistable nonlinear response of MEMS resonators. *Nonlinear Dyn.* **2017**, *90*, 1627–1645. [CrossRef]
31. Medina, L.; Gilat, R.; Ilic, B.R.; Krylov, S. Open-loop, self-excitation in a bistable micromechanical beam actuated by a DC electrostatic load. In Proceedings of the 2017 IEEE 30th International Conference on Micro Electro Mechanical Systems (MEMS), IEEE, Las Vegas, NV, USA, 22–26 January 2017; pp. 785–788.
32. Rajaei, A.; Vahidi-Moghaddam, A.; Ayati, M.; Baghani, M. Integral sliding mode control for nonlinear damped model of arch microbeams. *Microsyst. Technol.* **2019**, *25*, 57–68. [CrossRef]
33. Morozov, N.; Indeitsev, D.; Mozhgova, N.; Lukin, A.; Popov, I. *Equilibrium Forms of an Initially Curved Bernoulli–Euler Beam in Electric and Thermal Fields*; Doklady Physics; Springer: Berlin/Heidelberg, Germany, 2023; Volume 68, pp. 56–61.
34. Indeitsev, D.; Mozhgova, N.; Lukin, A.; Popov, I. Model of a Micromechanical Mode-Localized Accelerometer with an Initially Curved Microbeam as a Sensitive Element. *Mech. Solids* **2023**, *58*, 779–792. [CrossRef]
35. Younis, M.I.; Abdel-Rahman, E.M.; Nayfeh, A. A reduced-order model for electrically actuated microbeam-based MEMS. *J. Microelectromech. Syst.* **2003**, *12*, 672–680. [CrossRef]
36. Ouakad, H.M.; Younis, M.I. The dynamic behavior of MEMS arch resonators actuated electrically. *Int. J.-Non-Linear Mech.* **2010**, *45*, 704–713. [CrossRef]
37. Multiphysics, C. v. 5.2 a. COMSOL AB, Stockholm. Sweden, 2018. Available online: www.comsol.com (accessed on 4 March 2024).
38. Hajjaj, A.Z.; Alcheikh, N.; Younis, M.I. The static and dynamic behavior of MEMS arch resonators near veering and the impact of initial shapes. *Int. J.-Non-Linear Mech.* **2017**, *95*, 277–286. [CrossRef]
39. Alkharabsheh, S.A.; Younis, M.I. Statics and dynamics of MEMS arches under axial forces. *J. Vib. Acoust.* **2013**, *135*, 021007. [CrossRef]

Disclaimer/Publisher's Note: The statements, opinions and data contained in all publications are solely those of the individual author(s) and contributor(s) and not of MDPI and/or the editor(s). MDPI and/or the editor(s) disclaim responsibility for any injury to people or property resulting from any ideas, methods, instructions or products referred to in the content.